Hindawi
Wireless Communications and Mobile Computing
Volume 2021, Article ID 2566153, 11 pages
https://doi.org/10.1155/2021/2566153

Research Article

Vehicular Channel Characterization in Urban Environment at 30 GHz considering Overtaking and Traffic Flow

Yanzi Chen,[1] Lei Ma,[2] Xinjian Ou,[3] and Jingjing Liao[3]

[1]*Guangdong Communications & Networks Institute, Guangzhou 510670, China*
[2]*Tianjin University, Tianjin 300072, China*
[3]*Wuhan Maritime Communication Research Institute, Wuhan 430205, China*

Correspondence should be addressed to Lei Ma; 3142877286@qq.com

Received 13 September 2021; Accepted 10 November 2021; Published 13 December 2021

Academic Editor: Li Zhu

To realize reliable and stable millimeter-wave (mmWave) vehicular wireless communication, the research of vehicular channel characteristics in the dense urban environment is becoming increasingly important. A comprehensive research on the channel characteristics for 30 GHz vehicular communication in the Beijing Central Business District (CBD) scenario is conducted in this paper. The self-developed high-performance ray-tracing (RT) simulator is employed to support intensive simulations. Based on simulation results, the effects of multiantenna and beam switching on the key channel parameters are analyzed, as well as the impact of different traffic flows. The results can provide theoretical and data support for the evaluation of vehicular channel characteristics and will help for the design of the vehicular communication system enabling future intelligent transportation.

1. Introduction

With the rapid social development and progress, there are more and more vehicles all around the world [1]. In addition, the burden of urban traffic management is becoming heavier and heavier. The unceasing emergence of traffic jams, car crashes, and other problems on the road has brought enormous threats to the management and control of traffic systems on the road [2, 3]. The relevant departments have taken measures such as vehicle speed limit and road control to work out above-mentioned issues, but these measures are far from ensuring traffic safety. In the past few decades, with the deepening of global urbanization and industrialization, Intelligent Transportation Systems (ITS) have been developed rapidly [4]. ITS refers to the systems utilizing synergistic technologies and containing a series of applications that provides innovative services for various modes of transportation, which plays a vital part for modern society [1, 5]. For example, automatic road enforcement, dynamic traffic light sequence, and self-driving cars are all involved in ITS.

Therefore, ITS is a frontier project in the field of transportation research which can further improve the effectiveness of road traffic and the safety of vehicle driving, thus providing users with a more safe and reliable travel environment [6]. It is necessary to adopt ultrareliable, low-latency, and high-data-rate communications to realize various security-critical vehicle applications (such as car/road/lane/pedestrian/location detection) [6, 7]. As more sensors (radars, cameras, etc.) are embedded in the vehicle, the era of autonomous and intelligent driving has arrived [8, 9]. The number of sensors is so large that we need advanced wireless links that can support Gbit/s data rates to transmit the data from all the sensors [10]. However, current conventional technologies such as Dedicated Short-Range Communications (DSRC) (the maximum actual data rate comes up to only 2-6 Mbit/s) and fourth-generation (4G) cellular communication (the maximum data rate can reach only 100 Mbit/s at a high-speed mobile state, even much lower for actual data rate) are inadequate to deal with the Gbit/s data rates that are likely to be generated in next-generation of vehicles [10, 11]. The millimeter-wave (mmWave) band

can effectively improve the shortage of traditional spectrum resources and better serve the future intelligent urban transportation [12, 13]. Therefore, the propagation characteristics of mmWave in vehicular communication are important foundations to provide guidelines for channel modeling and communication system design.

The differentiation of vehicle-to-vehicle (V2V) channel characteristics with the consideration of the same region and different traffic flow and speeds at 5.9 GHz were concerned in the research of [14]. [15] carried out measurements of actual V2V channel obstructed by large vehicles at 5.9 GHz. [16] proposed a V2V channel model which considers the propagation mechanisms including the line-of-sight, the rays of single and double bounced when local scatterers are moving in the light of random velocities and directions. By means of measurement-calibrated ray-tracing (RT) simulations, the obstructive V2V channels were characterized in [17]. [18] proposed the hybrid model, and it is the first numerical simulation model which can model the diffuse reflection in the tunnel and has true time-variant temporal relativity for a link of nonstationary V2V communication. [19] showed the non-wide-sense stationary geometry-based model in which there are both immobile and mobile scatterers for V2V Multiple-Input Multiple-Output (MIMO) Ricean fading channels. The authors in [20] proposed analytical models of IEEE 802.15.4 non-beacon-enabled mode for Internet of Vehicle (IoV) with the consideration of the IoV application features. [21] demonstrated the three-dimensional (3D) cluster-based nonstationary channel model of V2V communications. [22] proposed a model of nonisotropic scattering V2V Ricean fading channels that is generic geometry-based stochastic. [23] investigated the charging mechanism with flexibility and efficiency applied to electric vehicles. Aiming at the nonisotropic MIMO V2V Ricean fading channels, [24] proposed a new 3D theoretical regular-shaped geometry-based stochastic model (RS-GBSM) and the corresponding sum-of-sinusoid (SoS) simulation models. [25] came up with a resource allocation strategy to improve the security of the physical layer of the vehicle communication networks.

Thus, there is still a further investigation value for various vehicular scenarios at more mmWave bands. Furthermore, the design of mmWave channel should contain both the received power, and the realization of high-resolution in the time and spatial domain [26]. It is indispensable to take the influence of the antenna position, antenna direction, multiantenna, beam switching, and the surrounding objects into the design of mmWave vehicular channels.

In this paper, the vehicular channel characteristics are comprehensively studied at 30 GHz for the urban Central Business District (CBD) scenario in Beijing city. The high-performance Cloud-computing Ray-Tracing platform (CloudRT) [27] is applied to carry out intensive simulations for the urban scenario with extensive moving vehicles. RT simulation is a deterministic wireless channel modeling method that can offer complete information about multipath effects in the time, frequency, and spatial domain, which contributes to establishing an accurate channel model of the specific location. It has been successfully applied to various works and researches. The authors in [28] proposed to carry out virtual drive testing (VDT), by reproducing RT-simulated channels by means of the field synthesis technology. The results generated from RT simulations of interior scenes for a penetrable hollow wedge formed by multilevel walls can correspond to that of the 3D full wave [29]. [30] presented many kinds of methods for direct optimization with regard to point-to-point ionospheric RT. Users can generate their own channel according to their own needs by reconstructing the 3D model of the scenario and setting up simulation parameters (frequency, antenna pattern, etc.) in the CloudRT. For additional information about the CloudRT, please refer to the tutorial [27] and the official website. This paper makes the following main contribution:

(i) The mmWave vehicular channel characteristics are analyzed with consideration of the impact of overtaking and simulation configurations, including different antenna directions and various traffic flows. The effects of multiantenna and beam switching of the receiver (Rx) are evaluated under overtaking situation

(ii) On the basis of the RT simulation results, the analysis of RMS delay spread, Rician K-factor, and angular spread is conducted, which can contribute to understanding the vehicular channel characteristics. In addition, it is helpful for a designer to design and evaluate the vehicular communication system enabling ITS

The rest of this paper is structured as follows: The scenario modeling and the simulation configurations are described in Section 2. Key channel parameters are characterized and analyzed in Section 3. At last, a comprehensive conclusion is described in Section 4.

2. Simulation Configuration for Urban CBD Scenario

2.1. Overview of the Simulation Scenario. The RT simulations in this paper are realized based on the three-dimensional (3D) environment models that are rebuilt from OpenStreetMap (OSM) for Beijing CBD. OSM is a free and editable world map service jointly created by the Internet public. It can provide not only street map information but also 3D building information. Our team developed a plugin which is an entirely open-source software for accessing the OSM data more conveniently.

A typical urban street area (i.e., CBD) in Beijing is selected as the simulation scenario (see Figure 1). As shown in Figure 2, based on the map information of the selected area from OSM, the 3D urban scenario for Beijing CBD is reconstructed with the help of the SketchUp tool. Both street and building information from OSM data can be imported into SketchUp through the plugin directly. In the Beijing CBD scenario, the geometry of objects is taken into account and corresponding materials are allocated to the surfaces of each object. In order to reconstruct the real urban street

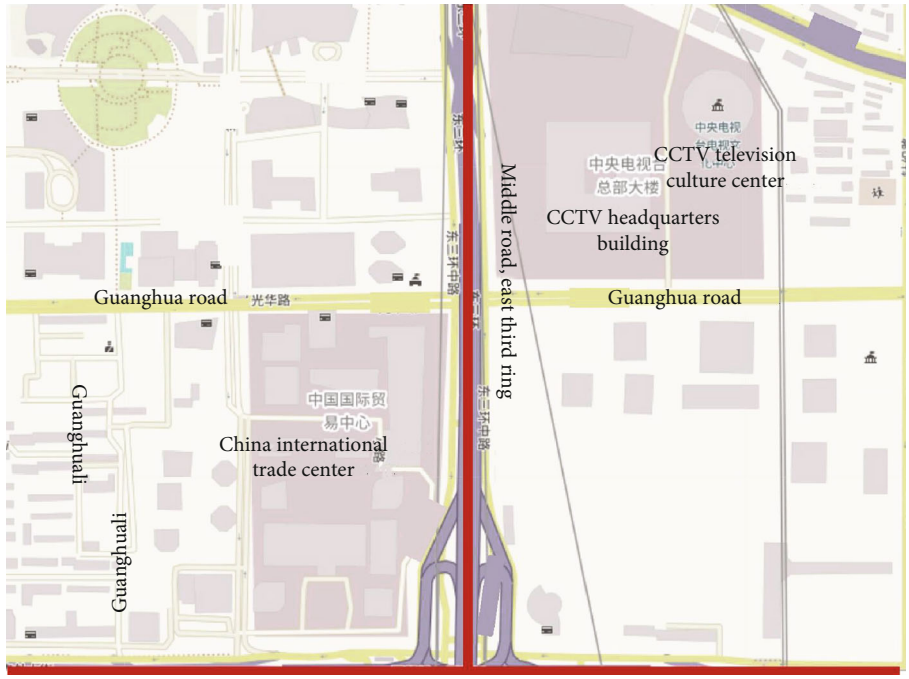

Figure 1: Beijing CBD map in OpenStreetMap.

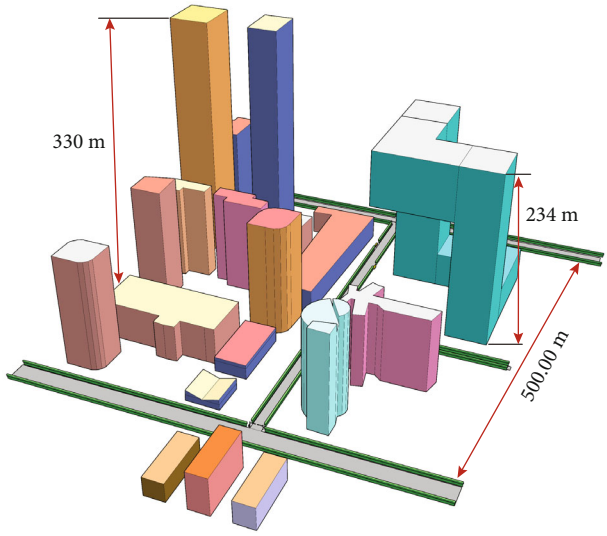

Figure 2: 3D model of an urban scenario in the RT simulations.

scenario, roadside trees, bus stations, and other common small-scale objects (i.e., traffic lights/signs) are all considered in the modeling.

2.2. Vehicle Types. According to the 3GPP TR 37.885 standard [31], three typical vehicle types in urban scenario are considered in this paper. The size of the vehicles and their distribution (i.e., the percentage of all vehicles) on the road are shown in Table 1. The 3D models of vehicles built by the SketchUp tool are shown in Figure 3.

One 4-lane road with a 3.5 m width of each lane is set in the scenario, and the vehicles of each lane are randomly generated based on the vehicle distribution. On each lane, vehicles travel at a constant speed and in a fixed direction, as shown in Figure 4. The bus installed Rx, i.e., the vehicle user equipment (UE) travels 500 m in the scenario. The number of sampling snapshots is appointed as 720, which corresponds to the sampling distance of 0.694 m.

Table 1: The size of three vehicle types and the distribution.

Vehicle type	Bus	Passenger car	Delivery van
Length	12 m	5 m	11 m
Width	2.55 m	2 m	2.6 m
Height	3.2 m	1.6 m	2.8 m
Distribution	20%	60%	20%

2.3. Simulation Configuration. The transmitter (Tx) and the Rx adopt the same antenna (as depicted in Figure 5). The emission power of the Tx is 20 dBm. The maximum antenna gain of the Tx and the Rx is 22 dBi. The propagation mechanisms are direct ray, reflection (up to 2nd order), and scattering (single-lobe directive scattering model). The Rx multiantenna at vehicle user equipment (UE) is installed on the top of the bus head with a total height of 3.25 m, which contains the bus height (3.2 m) and the antenna bracket. The antenna patterns of the three beams are the same, and the angle between two adjacent beams is 20° (as depicted in Figure 6).

For the "overtaking" cases in the RT simulations, the Tx is assembled on a building of one side of the road, with its main lobe pointing to the center of the 500 m road end, as shown in Figure 7. At the beginning, the bus is driven in the slow lane (vehicle speed of 15 km/h); then, the bus turns to the fast lane (vehicle speed of 25 km/h) by degrees. After

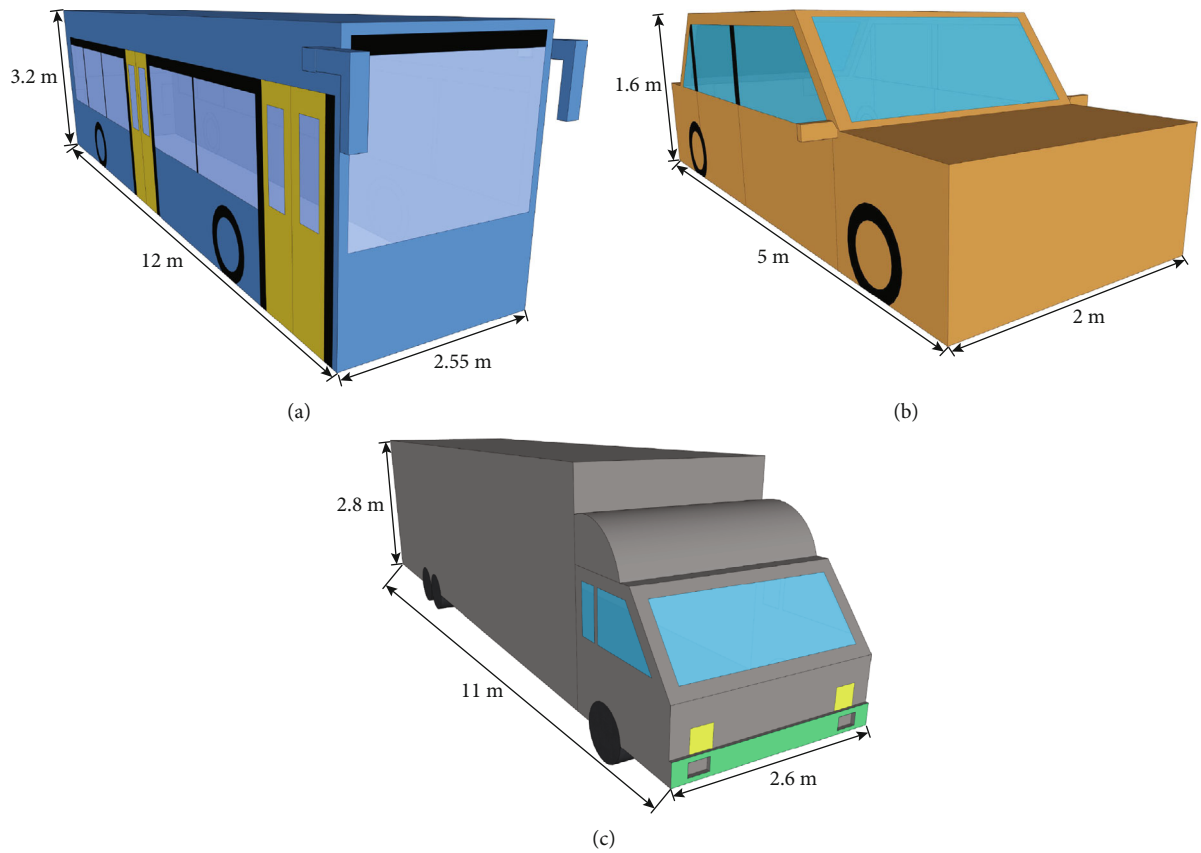

Figure 3: 3D models of three vehicle types in the RT simulations: (a) bus; (b) passenger car; (c) delivery van.

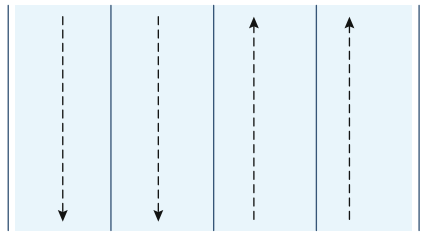

Lane	1	2	3	4
Speed (km/h)	15	25	25	15

Figure 4: Four-lane road in the urban scenario.

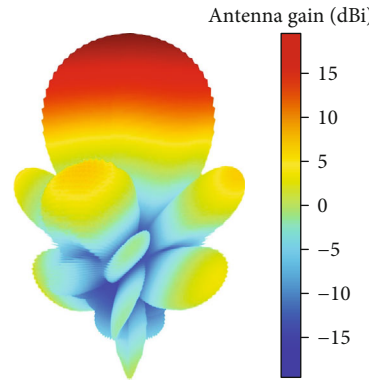

Figure 5: Tx antenna pattern and Rx antenna pattern in the RT simulations.

overtaking preceding vehicle, the bus comes back to the slow lane.

As shown in Figure 8, the specific overtaking trajectory can be divided into three sections: (1) "A-B" section: the vehicle UE in the slow lane turns to the adjacent fast lane through two arc trajectory; (2) "B-C" section: the vehicle UE drives in the fast lane for a period of time, exceeding the previous vehicle for a certain distance; (3) "C-D" section: the vehicle UE returns to the original slow lane through two arc trajectories in the same way; then, the overtaking process is completed. In Figure 8, r is the minimum turning radius of the bus (160 m in this simulation), and θ is the central angle corresponding to a section of arc trajectory in the turning process.

In the process of turning from slow lane to fast lane, the speed of the vehicle UE accelerates evenly from the speed of slow lane to the speed of fast lane. After turning to the fast lane, the vehicle UE drives at a uniform speed of the fast lane (i.e., 25 km/h) for a period of time to achieve overtaking. The process of returning to the slow lane after overtaking is just the opposite. The vehicle UE decelerates evenly from 25 km/

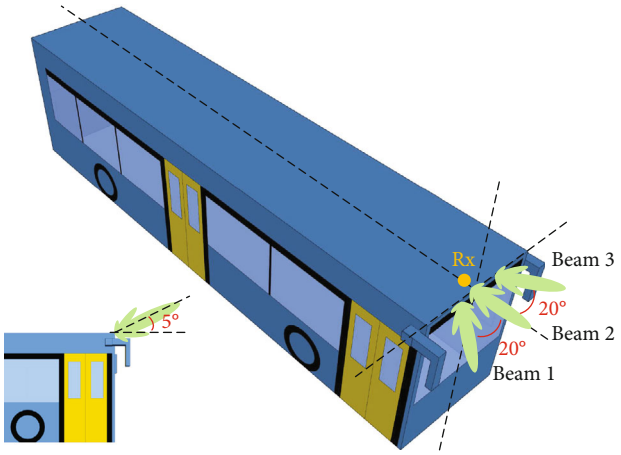

Figure 6: Locations of the Rx multiantenna on the bus.

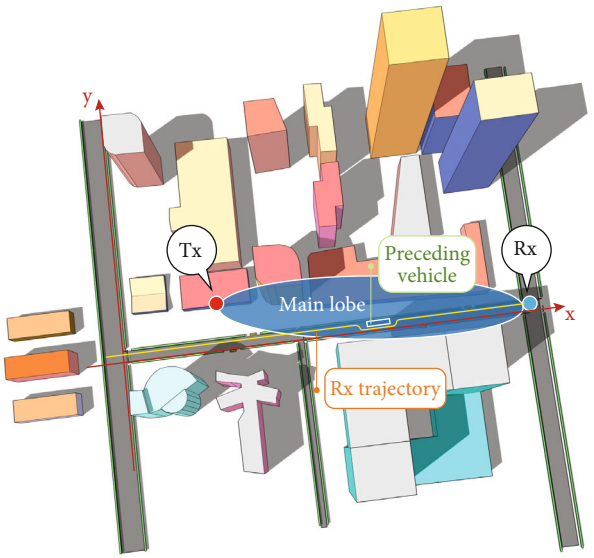

Figure 7: Overtaking scenario in the RT simulations.

h to 15 km/h; after being back to the slow lane, it continues to drive as 15 km/h.

For the "various traffic flow" cases in the RT simulations, the Tx is assembled on the building at the beginning of the 500 m road (Tx height is 15 m), whose main lobe points to the center of the 500 m road end, as shown in Figure 9. Three different traffic flows are considered: 10%, 50%, and 90% (the number of vehicles on the road is 10%, 50%, and 90% of the number of total randomly generated vehicles).

In the cases of "overtaking," multi-antenna and beam switching (Beam 1-3) techniques on the Rx are adopted. In the cases of "different traffic flows," the influence of different traffic flows (10%, 50%, and 90%) on Beam 2 is mainly studied. As listed in Table 2, six cases are simulated. The specific simulation configuration for all cases is summarized in Table 3.

The electromagnetism (EM) parameters of related materials were previously measured and calibrated [32–34], which are listed in Table 4. ε_r' corresponds to the real component of the relative permittivity, $\tan\delta$ corresponds to the loss tangent, and S and α are the coefficient and exponent of scattering in the directive scattering model [35].

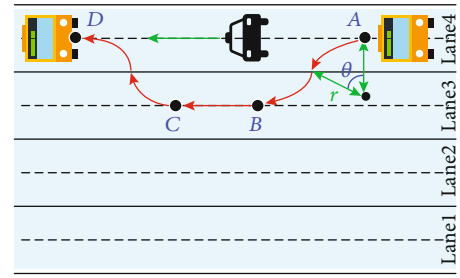

Figure 8: Overtaking trajectory in the RT simulations.

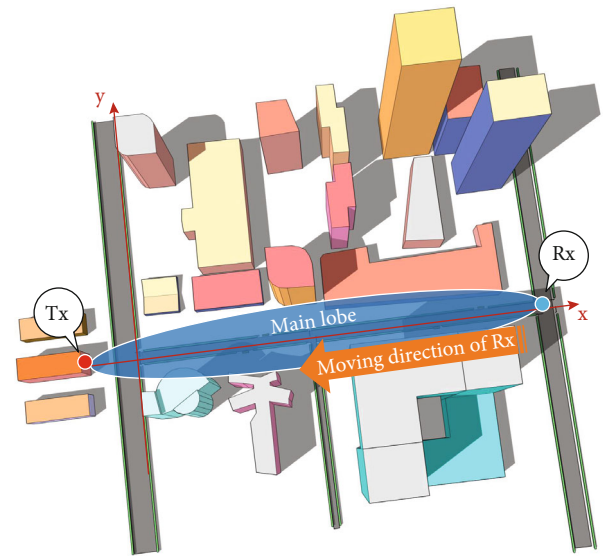

Figure 9: Various traffic flows in the RT simulations.

Table 2: Total cases in the RT simulations.

Situation	Traffic flow	Rx beam	Case
Overtaking	50%	Beam 1	OT-Beam 1
		Beam 2	OT-Beam 2
		Beam 3	OT-Beam 3
Various traffic flows	10%	Beam 2	TF-10%
	50%		TF-50%
	90%		TF-90%

3. Channel Parameterization Based on RT Simulations

On the basis of simulation results, the vehicular channel for the overtaking situation and different traffic flow situation is characterized by means of the following relevant significant parameters: received power, RMS delay spread, Rician K -factor, and angular spreads.

3.1. Overtaking Situation. For the overtaking situation, the received power is analyzed based on the whole motion

Table 3: Simulation configuration for Beijing CBD scenario.

Frequency range	29.5 GHz-30.5 GHz	
Frequency step	1 MHz	
Tx	Antenna type	Directional antenna
	Power	20 dBm
	Antenna gain	22 dBi
Rx	Antenna type	Directional antenna
	Angle between two adjacent beams	20°
	Antenna gain	22 dBi
Propagation mechanism	Direct	✓
	Reflection	Up to the 2nd order
	Scattering	Single-lobe directive scattering
Material	Buildings	Brick, marble, toughened glass
	Urban furniture, vehicles	Metal
	Tree	Wood
	Ground	Granite

Table 4: EM parameters of diverse materials used in ray-tracing simulations.

Material	ε_r'	tan δ	S	α
Marble	3.0045	0.2828	0.0022	15.3747
Toughened glass	1.0538	23.9211	0.0025	5.5106
Brick	1.9155	0.0568	0.0019	49.5724
Metal	1	10^7	0.0026	17.7691
Wood	6.6	0.9394	0.0086	13.1404
Concrete	5.4745	0.0021	0.0011	109

process of the vehicle UE, while other parameters (i.e., RMS delay spread, Rician K-factor, and angular spreads) are extracted based on the motion process when the main lobe of the Rx antenna is inside the main lobe of the Tx antenna (the time of this motion process is snapshot 134-191).

The channel parameters are all fitted by the normal distribution for quantifying the channel parameters, and the fitting values of the normal distribution (mean value and standard deviation) are given in Table 5.

3.1.1. Received Power and Power Delay Profiles. For the overtaking situation, the received power is depicted in Figure 10, in which the blue/red/green solid lines represent the received power of the Beam 1/2/3, respectively. Moreover, the power delay profiles (PDPs) for Beam 2 are depicted in Figure 11. The overtaking occurs at snapshot 116 and ends at snapshot 226: the vehicle UE in the slow lane turns to the adjacent fast lane from snapshot 116 to snapshot 158 ("A-B"), it drives in the fast lane between snapshot 159 and snapshot 183 ("B-C"), and it returns to the original slow lane from snapshot 184 to snapshot 226 ("C-D").

Table 5: Extracted channel parameters for overtaking situation.

Beam	Beam 1	Beam 2	Beam 3
KF			
μ_{KF}(dB)	23.8349	18.8609	5.1248
σ_{KF} (dB)	10.8922	8.4369	12.2766
DS			
μ_{DS} (ns)	1.0294	2.5150	8.9078
σ_{DS} (ns)	0.8513	2.0200	3.9059
ASA			
μ_{ASA} (°)	5.4738	22.5876	111.8803
σ_{ASA} (°)	8.6889	21.8856	48.7490
ASD			
μ_{ASD}(°)	12.0010	8.9600	9.5934
σ_{ASD} (°)	21.1292	14.9146	12.9316
ESA			
μ_{ESA} (°)	1.1211	0.7682	7.7528
σ_{ESA} (°)	0.6750	0.5118	3.2560
ESD			
μ_{ESD} (°)	0.9952	1.1564	2.8478
σ_{ESD} (°)	1.4500	1.0810	1.0756

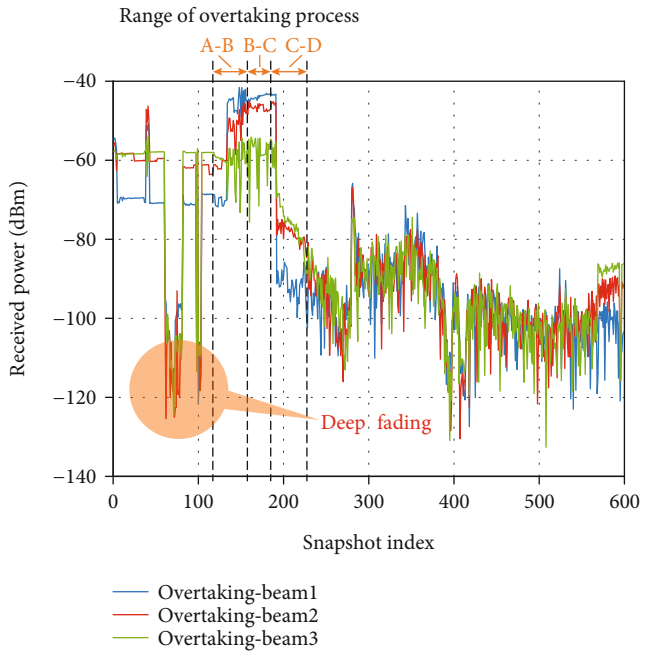

Figure 10: Received power for the overtaking situation.

As depicted in Figure 10, when the overtaking has not occurred, the received power of Beam 2 (red solid lines) is greater than that of Beam 1 (blue solid lines). For all the three beams, it is patently obvious that there exists deep fading in two consecutive periods when the snapshots are approximately 61-81 and 98-103, respectively (see Figures 10 and 11). The deep fading results from the fact that there is no direct

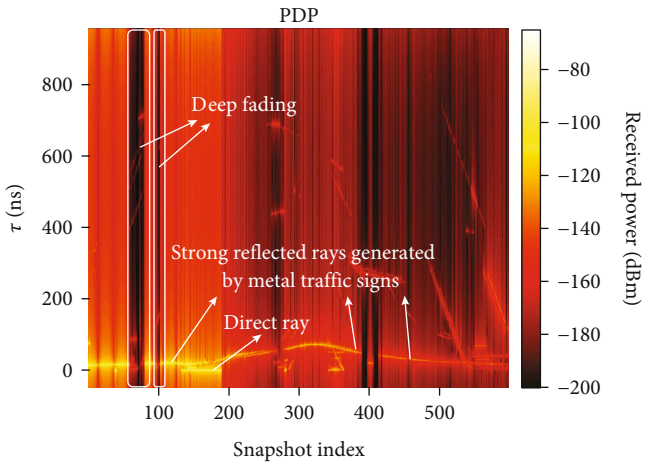

Figure 11: PDP of the Beam 2 for the overtaking situation.

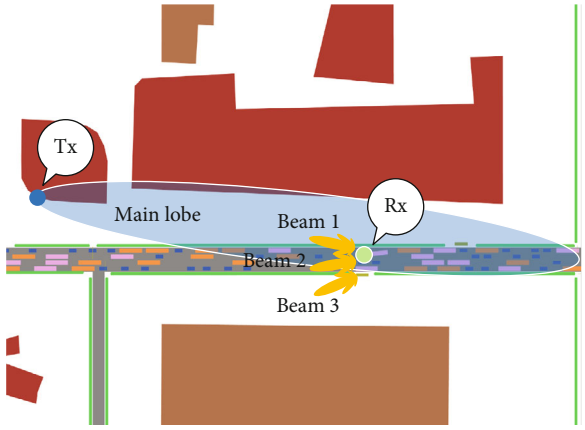

Figure 12: Schematic diagram for antenna main lobe for the Tx and Rx when vehicle UE is steering in the first section of the overtaking process.

ray or strong reflected ray between the Tx and Rx in these two periods.

In the first section of the overtaking process (i.e., "A-B"), with the direction rotation of the bus, the main lobe of Beam 2 diverges from the main lobe of the Tx gradually, while the main lobe of Beam 1 aligns with the main lobe of the Tx gradually (as depicted in Figure 12). Therefore, the received power of Beam 1 gradually surpasses that of Beam 2. Then, the bus proceeds to drive on the fast lane and approaches the Tx gradually (i.e., "B-C"), the received power of Beam 1 is always greater than the received power of Beam 2 because the main lobe of Beam 1 is aligned with the main lobe of Tx, and the main lobe of Beam 2 is more and more deviated from the main lobe of Tx.

In the last section of the overtaking process (i.e., "C-D"), similar to the first section, the main lobe of Beam 1 and Beam 2 seriously diverges from the Tx main lobe, only the main lobe of Beam 3 fractionally aligns with the Tx main lobe (as depicted in Figure 13). Therefore, the received power of Beam 3 (green solid lines) is greater than

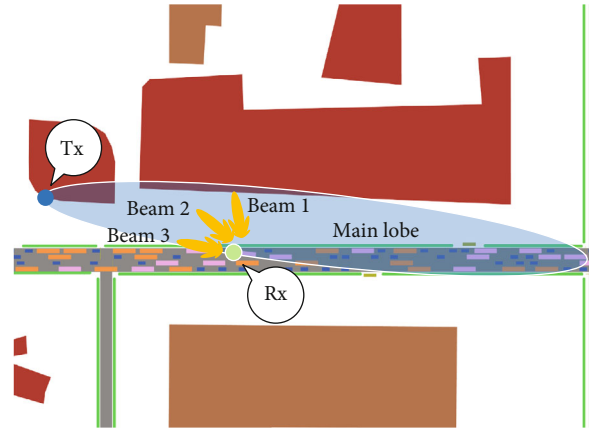

Figure 13: Schematic diagram for the antenna main lobe of Tx and Rx when vehicle UE is steering in the last section of the overtaking process.

that of Beam 1 and Beam 2. Actually, from about snapshot 183, as the vehicle UE leaves the main lobe of the Tx by degrees, the received power for all the three beams begins to decline.

3.1.2. Rician K-Factor. The value obtained by dividing the power of the strongest ray by the sum of the remaining rays' power is recorded as the Rician K-factor, which can be calculated using the following formula [36, 37]:

$$\mathrm{KF(dB)} = 10 \bullet \log_{10} \frac{\left| E_{r_1} e^{j\varphi_{r_1}} \right|^2}{\left| \sum_{r_i} E_{r_i} e^{j\varphi_{r_i}} - E_{r_1} e^{j\varphi_{r_1}} \right|^2}, \quad (1)$$

where Rician K-factor is abbreviated as KF, the electric field of each ray is expressed by means of amplitude E_{r_i} and phase φ_{r_i}, and $E_{r_1} e^{j\varphi_{r_1}}$ refers to the electrical field of the strongest ray [38]. The cumulative distribution functions (CDFs) of KF in the simulations for the overtaking situation are shown in Figure 14.

According to Table 5 and Figure 14, the Rician K-factor of Beam 1 is obviously the largest. This is because, in the overtaking process, the main lobe of Beam 1 is aligned with the Tx main lobe for the longest time compared with Beam 2 and Beam 3, resulting in a greater power contribution of the direct path than other multipaths.

Contrarily, the Rician K-factor of Beam 3 is the smallest, whose values are less than 0 dB in approximately 20% probability. This indicates that the received power of the direct path of Beam 3 is very small and even less than the sum of other multipath components at certain snapshots, which is caused by the misalignment between the main lobe of Beam 3 and the Tx.

3.1.3. RMS Delay Spread. RMS delay spread can quantify the dispersion effect in the time delay domain, whose definition

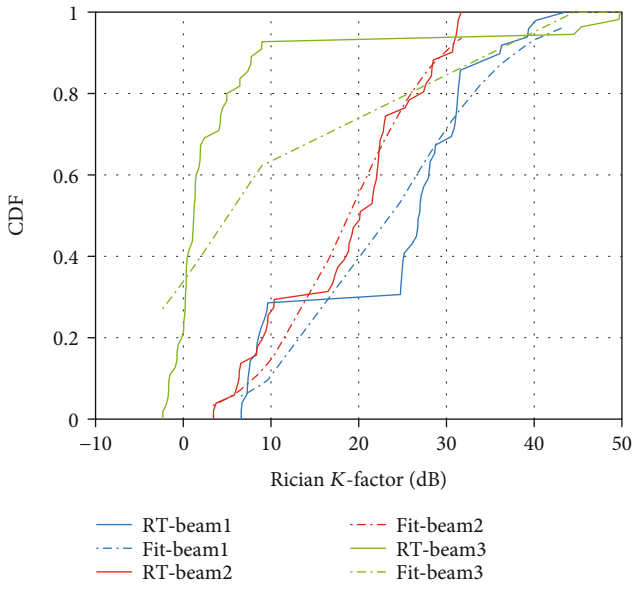

Figure 14: CDFs of Rician K-factor for the overtaking situation.

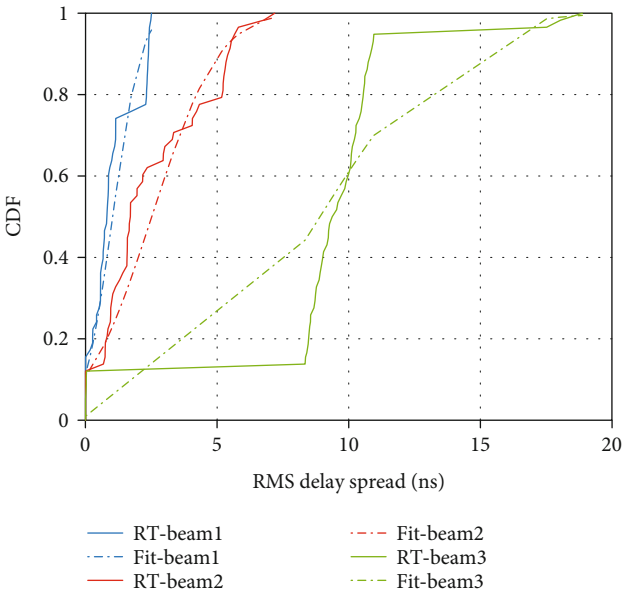

Figure 15: CDFs of RMS delay spread for the overtaking situation.

is the square root of the second central moment of the power delay profile (PDP) [39]:

$$\sigma_\tau = \sqrt{\overline{\tau^2} - \bar{\tau}^2}, \tag{2}$$

where σ_τ represents the RMS delay spread. $\overline{\tau^2}$ and $\bar{\tau}$ can be calculated by the following formula, respectively:

$$\begin{aligned} \overline{\tau^2} &= \frac{\sum_{r_i} \tau_{r_i}^2 \bullet P_{r_i}}{\sum_{r_i} P_{r_i}}, \\ \bar{\tau} &= \frac{\sum_{r_i} \tau_{r_i} \bullet P_{r_i}}{\sum_{r_i} P_{r_i}}, \end{aligned} \tag{3}$$

where P_{r_i} is the power of the r_i multipath and τ_{r_i} is the excess time delay. Obviously, for the direct path, the time delay $\tau_{r_i} = 0$. The CDFs of RMS delay spread for the overtaking situation are shown in Figure 15.

According to Table 5 and Figure 15, the μ_{DS} of Beam 3 is 8.91 ns, which is larger than the μ_{DS} of Beam 1 and Beam 2. This can be verified by the simulation results: the metal traffic signs and bus stations on both sides of the road produce more reflected rays, reaching the main lobe of Beam 3 and resulting in the increase of the RMS delay spread.

3.1.4. Angular Spreads. ASA/ASD and ESA/ESD indicate the distribution of the azimuth angles and elevation angles for each departure path from the Tx and each arrival path to the Rx, respectively. The angular spreads are acquired based on 3GPP standards [40]. The normal distribution fitting values of angular spreads for each beam are summarized in Table 5.

It is noticeable that the values of ASA and ASD are greater than ESA and ESD for all the three beams, which implies that the multipaths arrive from the horizontal direction in most of the cases. This phenomenon corresponds to the simulation results that a great quantity of reflected rays principally comes from the roadside buildings, and the scattering happens primarily on the surface of the moving vehicles. Furthermore, compared with the Tx, scatterers are mainly concentrated around the Rx (abundant moving vehicles on the road), which results in the value of ASA and ESA greater than ASD and ESD in most cases. This is because the multipath components arriving at the Rx come from more directions, while the multipath components leaving the Tx are more concentrated around the direct path.

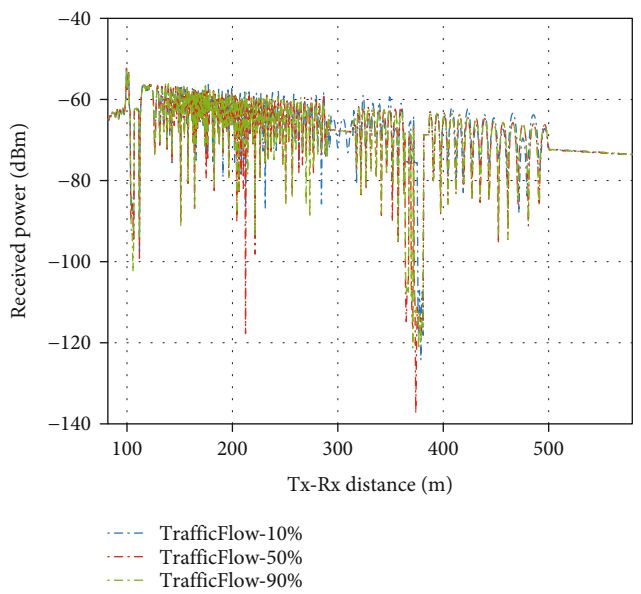

Figure 16: Received power for various traffic flows.

3.2. Various Traffic Flows

3.2.1. Received Power. The received power for various traffic flows in the urban scenario is depicted in Figure 16, where

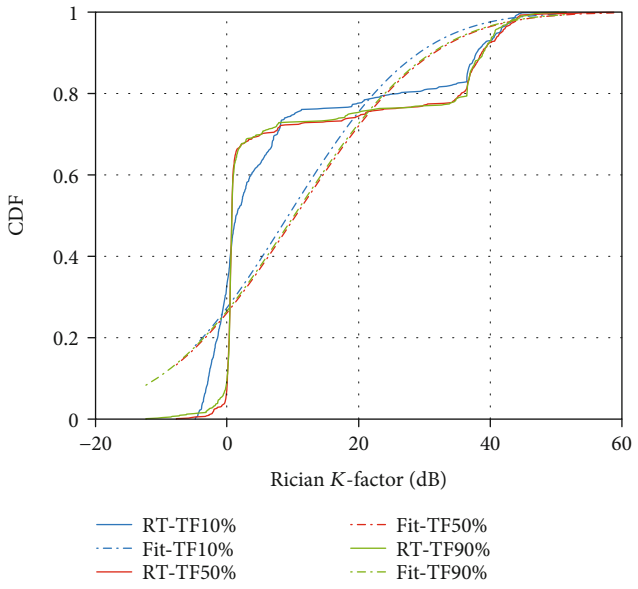

Figure 17: CDFs of Rician K-factor for various traffic flows.

the blue, red, and green dotted lines indicate the received power of the Rx when the traffic flow is 10%, 50%, and 90%, respectively.

As depicted in Figure 16, the received power has little difference under different traffic flows. The received power gradually decreases when the distance between the Tx and the Rx is increasing. This is due to the positive correlation between the free space path loss and the propagation distance; meanwhile, the vehicle UE gradually leaves the Tx main lobe, resulting in the power reduction of the direct path.

Moreover, the received power is more stable at higher traffic flow compared with low traffic flow, especially when the Rx moves further away from the Tx. This states clearly that there are more multipath components at the Rx due to the increase in the number of moving vehicles. The coherent superposition of these multipath components leads to the destructive combination of the field strength amplitude, which makes the oscillation of the received power no longer obvious.

3.2.2. Rician K-Factor. The CDFs of the Rician K-factor for various traffic flows are shown in Figure 17. The normal distribution fitting values of the Rician K-factor for various traffic flows are depicted in Table 6, including other critical channel parameters represented in the following subsections for various traffic flows.

It can be obtained from Figure 17 and Table 4 that with the raise of traffic flow, the values of the Rician K-factor change very little, which indicates that the traffic flow does not have a great impact on the Rician K-factor. This is because even if there are more multipath components with the raise of traffic flow, the sum of the power of all multipath components is still unable to compare with the power of the direct path.

3.2.3. RMS Delay Spread. The CDFs of RMS delay spread for various traffic flows are shown in Figure 18. As depicted in Figure 18 and Table 6, the mean value of RMS delay spread

Table 6: Extracted channel parameters for various traffic flows.

Traffic flows	10%	50%	90%
KF			
μ_{KF} (dB)	9.2821	10.4222	10.1698
σ_{KF} (dB)	15.4882	16.3482	16.3059
DS			
μ_{DS} (ns)	3.8350	7.3707	9.4804
σ_{DS} (ns)	9.4197	21.5488	32.5968
ASA			
μ_{ASA} (°)	5.8494	7.5269	7.3138
σ_{ASA} (°)	6.5465	12.2831	10.7081
ASD			
μ_{ASD} (°)	10.2406	5.8377	6.0284
σ_{ASD} (°)	7.8486	7.7034	7.9021
ESA			
μ_{ESA} (°)	1.8938	1.9491	1.8554
σ_{ESA} (°)	2.6339	6.7624	5.5535
ESD			
μ_{ESD} (°)	2.9221	4.0053	4.2447
σ_{ESD} (°)	6.2288	9.8575	10.8510

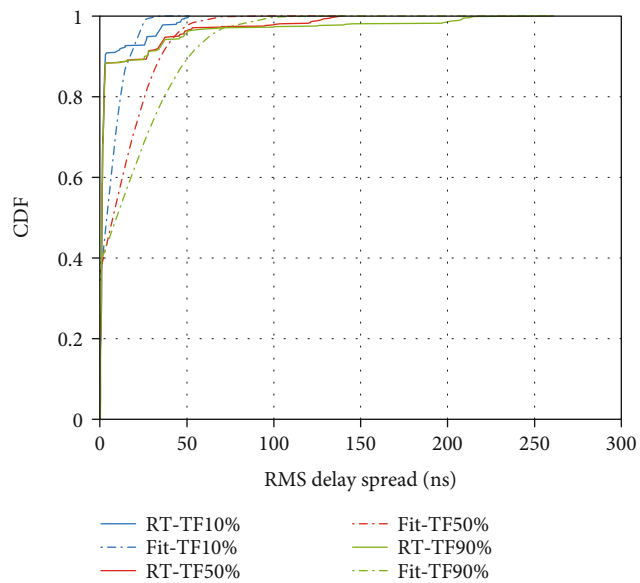

Figure 18: CDFs of RMS delay spread for various traffic flows.

increases (from 3.84 ns to 9.48 ns) with the increase of traffic flow, which is obviously due to the increase of multipath components generated from moving scatterers.

3.2.4. Angular Spreads. According to Table 6, we can find that with the raise of traffic flow, the mean value of ASA, ESA, and ESD does not change much; only the mean value of ASD decreases slightly.

4. Conclusions

In this paper, the vehicular channel at 30 GHz is characterized for Beijing CBD environment. The CloudRT platform is used to extract the key channel parameters of a realistic 3D urban scenario. Three different traffic flows (10%, 50%, and 90%), multiantenna, and beam switching (Beam 1, Beam 2, and Beam 3) are considered in RT simulations. The objects in the scenario are defined and reconstructed according to their typical geometries and materials. Channel characterization and respective conclusions are drawn based on simulation results.

In the process of overtaking, when the Tx is on the roadside, the maximum difference of the received power of three beams in different directions can be about 13 dB. With the direction rotation of the vehicle UE in the turning process, the original communication beam (the beam with the maximum received power before overtaking) gradually deviates from the main lobe of the Tx, resulting in its received power lower than that of other beams. Therefore, multiantenna and beam switching can be used to improve the reliability of the mmWave vehicular communication.

The channel parameters (Rician K-factor, RMS delay spread, and angular spreads) are affected by the direction of the antenna beam and the traffic flow on the road. In the case of low traffic flow (10%), the mean value of RMS delay spread is relatively small (3 ns), while in the case of high traffic flow (90%), the mean value of RMS delay spread is relatively large (9 ns), which is about three times of that in the case of low traffic flow. This is due to the increase of multipath components caused by the increase of mobile vehicles. In addition, the values of angular spreads in the urban scenario are affected by the moving vehicles to a certain extent. In general, the values of ASA and ASD are greater than ESA and ESD, which is due to most of the reflection and scattering originating from roadside buildings and moving vehicles. However, the values of the Rician K-factor are not sensitive to the change of traffic flow.

In conclusion, the channel characteristic analysis and the key channel parameters provided in this paper can help the research community understand the propagation channel when designing the mmWave communication system for future intelligent transportation.

Data Availability

The [DATA TYPE] data used to support the findings of this study are included within the article.

Conflicts of Interest

The authors declare that there is no conflict of interest regarding the publication of this paper.

Acknowledgments

This work was supported by the Key-Area Research and Development Program of Guangdong Province, China (2018B010124001).

References

[1] X. Chen, W. Xue, H. Shi, J. Yi, and W. E. I. Sha, "Orbital angular momentum multiplexing in highly reverberant environments," *IEEE Microwave and Wireless Components Letters*, vol. 30, no. 1, pp. 112–115, 2020.

[2] Y. Li, L. Zhu, H. Wang, F. R. Yu, and S. Liu, "A cross-layer defense scheme for edge intelligence-enabled CBTC systems against MitM attacks," *IEEE Transactions on Intelligent Transportation Systems*, vol. 22, no. 4, pp. 2286–2298, 2021.

[3] L. Zhu, Y. Li, F. R. Yu, B. Ning, T. Tang, and X. Wang, "Cross-layer defense methods for jamming-resistant CBTC systems," *IEEE Transactions on Intelligent Transportation Systems*, vol. 22, no. 11, pp. 7266–7278, 2021.

[4] L. Zhu, H. Liang, H. Wang, B. Ning, and T. Tang, "Joint security and train control design in blockchain empowered CBTC system," *IEEE Internet of Things Journal*, 2021.

[5] X. Xu, Y. Liu, W. Wang et al., "ITS-frame: a framework for multi-aspect analysis in the field of intelligent transportation systems," *IEEE Transactions on Intelligent Transportation Systems*, vol. 20, no. 8, pp. 2893–2902, 2019.

[6] C. Bila, F. Sivrikaya, M. A. Khan, and S. Albayrak, "Vehicles of the future: a survey of research on safety issues," *IEEE Transactions on Intelligent Transportation Systems*, vol. 18, no. 5, pp. 1046–1065, 2017.

[7] W. Wang, T. Jost, C. Gentner, S. Zhang, and A. Dammann, "A semiblind tracking algorithm for joint communication and ranging with OFDM signals," *IEEE Transactions on Vehicular Technology*, vol. 65, no. 7, pp. 5237–5250, 2016.

[8] D. Yan, K. Guan, D. He et al., "Channel characterization for vehicle-to-infrastructure communications in millimeter-wave band," *IEEE Access*, vol. 8, pp. 42325–42341, 2020.

[9] D. He, L. Wang, K. Guan, B. Ai, J. Kim, and Z. Zhong, "Channel characterization for mmWave vehicle-to-infrastructure communications in urban street environment," in *2019 13th European Conference on Antennas and Propagation (EuCAP)*, pp. 1–5, Krakow, Poland, 2019.

[10] J. Choi, V. Va, N. Gonzalez-Prelcic, R. Daniels, C. R. Bhat, and R. W. Heath, "Millimeter-wave vehicular communication to support massive automotive sensing," *IEEE Communications Magazine*, vol. 54, no. 12, pp. 160–167, 2016.

[11] V. Va, T. Shimizu, G. Bansal, and R. W. Heath, "Beam design for beam switching based millimeter wave vehicle-to-infrastructure communications," in *2016 IEEE International Conference on Communications (ICC)*, pp. 1–6, Kuala Lumpur, Malaysia, 2016.

[12] T. S. Rappaport, Y. Xing, G. R. MacCartney, A. F. Molisch, E. Mellios, and J. Zhang, "Overview of millimeter wave communications for fifth-generation (5G) wireless networks—with a focus on propagation models," *IEEE Transactions on Antennas and Propagation*, vol. 65, no. 12, pp. 6213–6230, 2017.

[13] L. Wu, D. He, K. Guan, B. Ai, J. Kim, and H. Chung, "Millimeter-wave channel characterization for vehicle-to-infrastructure communication," in *2020 14th European Conference on Antennas and Propagation (EuCAP)*, pp. 1–5, Copenhagen, Denmark, 2020.

[14] F. Li, W. Chen, Y. Shui et al., "5.9 GHz vehicular channels comparisons between two traffic status for dense urban area," *China Communications*, vol. 15, no. 4, pp. 58–71, 2018.

[15] M. Yang, B. Ai, R. He et al., "Measurements and cluster-based modeling of vehicle-to-vehicle channels with large vehicle

obstructions," *IEEE Transactions on Wireless Communications*, vol. 19, no. 9, pp. 5860–5874, 2020.

[16] X. Liang, W. Cao, and X. Zhao, "Doppler power spectra for 3D vehicle-to-vehicle channels with moving scatterers," *IEEE Access*, vol. 6, pp. 42822–42828, 2018.

[17] K. Guan, D. He, B. Ai et al., "5-GHz obstructed vehicle-to-vehicle channel characterization for internet of intelligent vehicles," *IEEE Internet of Things Journal*, vol. 6, no. 1, pp. 100–110, 2019.

[18] M. Gan, G. Steinböck, Z. Xu, T. Pedersen, and T. Zemen, "A hybrid ray and graph model for simulating vehicle-to-vehicle channels in tunnels," *IEEE Transactions on Vehicular Technology*, vol. 67, no. 9, pp. 7955–7968, 2018.

[19] H. Jiang, Z. Zhang, L. Wu, and J. Dang, "A non-stationary geometry-based scattering vehicle-to-vehicle MIMO channel model," *IEEE Communications Letters*, vol. 22, no. 7, pp. 1510–1513, 2018.

[20] C. Wang, C. Chou, P. Lin, and M. Guizani, "Performance evaluation of IEEE 802.15.4 nonbeacon-enabled mode for internet of vehicles," *IEEE Transactions on Intelligent Transportation Systems*, vol. 16, no. 6, pp. 3150–3159, 2015.

[21] Y. Li, R. He, S. Lin et al., "Cluster-based nonstationary channel modeling for vehicle-to-vehicle communications," *IEEE Antennas and Wireless Propagation Letters*, vol. 16, pp. 1419–1422, 2017.

[22] X. Cheng, C. Wang, B. Ai, and H. Aggoune, "Envelope level crossing rate and average fade duration of nonisotropic vehicle-to-vehicle Ricean fading channels," *IEEE Transactions on Intelligent Transportation Systems*, vol. 15, no. 1, pp. 62–72, 2014.

[23] R. Zhang, X. Cheng, and L. Yang, "Stable matching based cooperative V2V charging mechanism for electric vehicles," in *2017 IEEE 86th Vehicular Technology Conference (VTC-Fall)*, pp. 1–5, Toronto, ON, Canada, 2017.

[24] Y. Yuan, C. Wang, X. Cheng, B. Ai, and D. I. Laurenson, "Novel 3D geometry-based stochastic models for non-isotropic MIMO vehicle-to-vehicle channels," *IEEE Transactions on Wireless Communications*, vol. 13, no. 1, pp. 298–309, 2014.

[25] W. Yang, R. Zhang, C. Chen, and X. Cheng, "Secrecy-based resource allocation for vehicular communication networks with outdated CSI," in *2017 IEEE 86th Vehicular Technology Conference (VTC-Fall)*, pp. 1–5, Toronto, ON, Canada, 2017.

[26] T. Jost, W. Wang, and M. Walter, "A geometry-based channel model to simulate an averaged-power-delay profile," *IEEE Transactions on Antennas and Propagation*, vol. 65, no. 9, pp. 4925–4930, 2017.

[27] D. He, B. Ai, K. Guan, L. Wang, Z. Zhong, and T. Kürner, "The design and applications of high-performance ray-tracing simulation platform for 5G and beyond wireless communications: a tutorial," *IEEE Communications Surveys & Tutorials*, vol. 21, no. 1, pp. 10–27, 2019.

[28] W. Fan, I. Carton, P. Kyösti, and G. F. Pedersen, "Emulating ray-tracing channels in multiprobe anechoic chamber setups for virtual drive testing," *IEEE Transactions on Antennas and Propagation*, vol. 64, no. 2, pp. 730–739, 2016.

[29] C. H. Teh, B. K. Chung, and E. H. Lim, "Multilayer wall correction factors for indoor ray-tracing radio propagation modeling," *IEEE Transactions on Antennas and Propagation*, vol. 68, no. 1, pp. 604–608, 2020.

[30] I. A. Nosikov, M. V. Klimenko, G. A. Zhbankov, A. V. Podlesnyi, V. A. Ivanova, and P. F. Bessarab, "Generalized force approach to point-to-point ionospheric ray tracing and systematic identification of high and low rays," *IEEE Transactions on Antennas and Propagation*, vol. 68, no. 1, pp. 455–467, 2020.

[31] 3rd Generation Partnership Project, *TR 37.885-15.0.0 Study on Evaluation Methodology of New Vehicle-to-Everything (V2X) Use Cases for LTE and NR (Release 15)*, 2018.

[32] F. Wang and K. Sarabandi, "An enhanced millimeter-wave foliage propagation model," *IEEE Transactions on Antennas and Propagation*, vol. 53, no. 7, pp. 2138–2145, 2005.

[33] K. Guan, B. Ai, B. Peng et al., "Towards realistic high-speed train channels at 5G millimeter-wave band—part I: paradigm, significance analysis, and scenario reconstruction," *IEEE Transactions on Vehicular Technology*, vol. 67, no. 10, pp. 9112–9128, 2018.

[34] K. Guan, B. Ai, B. Peng et al., "Towards realistic high-speed train channels at 5G millimeter-wave band—part II: case study for paradigm implementation," *IEEE Transactions on Vehicular Technology*, vol. 67, no. 10, pp. 9129–9144, 2018.

[35] V. Degli-Esposti, F. Franco, M. Vitucci Enrico, and F. Gabriele, "Measurement and modelling of scattering from buildings," *IEEE Transactions on Antennas & Propagation*, vol. 55, no. 1, pp. 143–153, 2007.

[36] P. Tang, J. Zhang, A. F. Molisch, P. J. Smith, M. Shafi, and L. Tian, "Estimation of the K-factor for temporal fading from single-snapshot wideband measurements," *IEEE Transactions on Vehicular Technology*, vol. 68, no. 1, pp. 49–63, 2019.

[37] L. Bernadó, T. Zemen, F. Tufvesson, A. F. Molisch, and C. F. Mecklenbräuker, "Time- and frequency-varying K -factor of non-stationary vehicular channels for safety-relevant scenarios," *IEEE Transactions on Intelligent Transportation Systems*, vol. 16, no. 2, pp. 1007–1017, 2015.

[38] L. Ma, K. Guan, D. He, B. Ai, J. Kim, and H. Chung, "Influence of meteorological attenuation on the channel characteristics for high-speed railway at the millimeter-wave band," in *2020 International Conference on Information and Communication Technology Convergence (ICTC)*, pp. 128–131, Jeju, Korea (South), 2020.

[39] Rappaport and Theodore, *Wireless Communications: Principles and Practice*, 2002.

[40] 3rd Generation Partnership Project, *Spatial Channel Model for MIMO Simulations*, 2003.